SMALL-SCALE RAPID 3D PARTICLE TRACKING

Draft of February 6, 2023 at 12:49

BY

LIU HONG

ADVISOR: LEONARDO P. CHAMORRO

PROPOSAL OF PRELIMINARY EXAM

Urbana, Illinois

Table of Contents

Introduction

Time-resolved3D particle tracking(3D-PTV) is a powerful technique to investigate particle dynamics and complex fluid flows. For particle tracking in common volume(>10 cm), tomographic approach, which acquires depth information from multiple simultaneous perspectives on illuminated volumes, is a popular method due to its spatial resolution and flexibility in the investigation volume. Tomographic approach usually involves four steps, particle reconstruction, track initialization, prediction and optimization. Although previous researchers proposed advanced prediction and optimization method, such as iterative particle reconstruction (IPR) [Wieneke, 2012] and Shake-The-Box [Schanz et al., 2016], numerous ghost particle created during the triangulation limits its application in industry area. This study first gets inspired by optimizing 4 views triangulation task, which is further described in Patallelized DLT chapter. The sustained progress on microfabrication techniques in the last couple of decades has opened new possibilities for microfluidics and, in particular, the design of biomedical devices and control of processes, including cooling [Singhal et al., 2004], mixing [Song and Ismagilov, 2003, Liu et al., 2004], extraction [Hisamoto et al., 2001, Kluge et al., 2009] and drug delivery [Tsai and Sue, 2007, Nguyen et al., 2013]. Hence, demands of tracking particle in small volume have increased. In order to overcome illumination and space constraints, techniques based on standard particle tracking, such as holographic [Sheng et al., 2006, Soria and Atkinson, 2008, Memmolo et al., 2011, Daloglu et al., 2018], confocal [Kinoshita et al., 2007, Lima et al., 2008], stereoscopic [Lindken et al., 2006, Bown et al., 2006] and defocus-based [Yoon and Kim, 2006, Pereira et al., 2007] variants; see discussion in Wereley and Meinhart [2010]. Development of microlens manufacturing technology and camera sensing allows for distinct possibilities for taking advantage of the so-called light field, LF [Gershun, 1939], which describes the distribution of light rays in space instead of 2D projection, in plenoptic function models [Adelson et al., 1991].

Light field cameras have been used in photography [Levoy and Hanrahan, 1996, Ng, 2005], computer vision [Tao et al., 2013, Adelson and Wang, 1992] and robotic navigation [Kaveti and Singh, 2020], among others. Belden et al. [2010] used concepts of LF imaging in a large camera array to capture multiple views simultaneously. Unlike tomo-PIV, Belden et al. [2010] performed synthetic aperture refocusing, which was

coined as synthetic aperture particle image velocimetry, SA-PIV, by using a map-shift-average algorithm. The large number of cameras needed may make it relatively bulky and costly.

Instead of considering a multi-camera approach, the use of microlens array, MLA, into the optical train of a conventional microscope [Levoy et al., 2006] has enabled the application span of LF to micro scale with a single, high-resolution camera. LF also has several advantages compared to SA-PIV or tomo-PIV. Indeed, the camera spatial calibration process, which is difficult in microscopic measurements, is unnecessary when MLA is pre-calibrated with a CCD or CMOS sensor. The relative independence of the main optic system leads to the LF technique being widely applied to a variety of microscopes and macro lenses and providing robust 3D data. Single-camera light field micro particle velocimetry, LF-PIV, proposed by Lynch et al. Lynch et al. [2012] became a popular complementary approach for space-constrained measurements [Shi et al., 2016b,a, 2017, Fahringer et al., 2015, Xu et al., 2017, Li et al., 2017]. Indeed, there are other single-camera methods, such as digital holography. Unfortunately, comparatively high-power laser requirement [Hinsch, 2002] and low signal-to-noise ratio [Ooms et al., 2009], and long reconstruction time may limit applications.

Despite this, several bottlenecks limit the capability and development of LF-PIV. One of the main drawbacks is the high computational cost during 3D reconstruction. Like conventional tomo-PIV, the space is discretized into cubic voxels with associated intensity and optic system project $E(x, y, z)$ onto 2D pixel-wise intensity distribution $I(x, y)$ [Fahringer et al., 2015], as follows:

$$\sum_{j \in N_i} w_{i,j} E\left(x_j, y_j, z_j\right) = I\left(x_i, y_i\right), \tag{1}$$

where N_i indicates the number of voxels in the line-of-sight of the $i-$th pixel, and $w_{i,j}$ represents a weighting coefficient dependent on the optic system. This is an ill-posed problem caused by an under-determined system of equations. A special series of algorithms known as algebraic methods that iteratively solve this linear equation system were introduced by Herman and Lent [1976]. For example, the standard multiplicative algebraic reconstruction technique, MART, proposed by Belden et al. [2010] is widely utilized with appropriate modifications to calculate the voxel intensity:

$$E\left(x_j, y_j, z_j\right)^{k+1} = E\left(x_j, y_j, z_j\right)^k \left(\frac{I\left(x_i, y_i\right)}{\sum_{j \in N_j} w_{i,j} E\left(x_j, y_j, z_j\right)^k}\right)^{\mu w_{i,j}}. \tag{2}$$

Here, k is the iteration number, and μ is a relaxation factor. Many pixels can capture one voxel, leading to an extended processing time in the weight matrix calculation and iterative steps. For instance, saving non-zero values of a $300 \times 200 \times 200$ voxels and 850×850 pixels weighting matrix requires approximately

350 GB, which is substantial for standard computers. 3D reconstruction for low-resolution image examples may still take on the order of an hour on a 12-core workstation with RAID 0 solid-state disk array. Other methods, including the so-called dense ray tracing-based MART [Shi et al., 2017] and pre-recognition simultaneous algebraic reconstruction technique [Zhu et al., 2021], have been proposed to improve the efficiency of reconstruction. However, the assessment of the weighting matrix bottleneck remains significant.

Consider sparse particle concentration characteristic for small-scale particle tracking and orthographic view of microscope, Levoy et al. [2006] and Truscott et al. [2017] utilized a 3D deconvolution algorithm to remove blurring effects in the images focal stack. Compared to algebraic methods, 3D deconvolution is efficient since it avoids storing large weighting matrices. However, iterative deconvolution such as the Richardson-Lucy algorithm [Sibarita, 2005] uses substantial computational power to store a focal stack of images and perform voxel-wise deconvolution. Like the kernel of deconvolution, point-spread-function (PSF) estimation needs the absence of noise and aberrations by empirically refocusing a sub-resolution fluorescent particle at the center of a lenslet [Levoy et al., 2006]. It may not be convenient to image sub-resolution fluorescent particle with the same optical system as a PIV setup, leading to inappropriate PSF estimation. PSF is not invariant to translation, making it inappropriate to use one PSF to deconvolve all voxels [Zhu et al., 2021]. Regardless of the performance of the algorithm, alignment between pixels of sub-images and MLA, which ensure a consistent square matrix of pixels underneath each lenslet and MLA rotated to axis-align with the camera sensor, is difficult to achieve during calibration due to lens distortion and fall of intensity towards the periphery of an image [Piller, 2012].

Here, this study extends the application of non-terative ray tracing 3D microscale particle tracking (Microscale Particle Tracking) to cm-scale since fluid field and particle motion and particle motion are more complex and harder to simulate compare to microscale. Cm-scale 3D Particle Tracking describes the major challenges faced for using this approach with perspective view system.

Parallelized DLT - Inspire

In this work, 4 calibrated camera system was employed to acquire 3D trajectories of grains inside the harvester to optimize the shelling and separating process. Charuco board [An et al., 2018] based intrinsic

and extrinsic calibration method was used to simplify calibration procedure and improve the robustness. Parallelized direct linear transformation (DLT) was utilized to remove the ghost particles and compute the 3D position of particle candidates. This algebraic 4 ray intersection method inspires later works of N rays intersection approach.

Experiment Setup and Principal Of 3D Tracking

4 a2A1920-160umBAS camera were mounted to capture image sequences for investigation volume from various view points. The camera system was calibrated by capturing 1000 frames of 7×10, grid size 20 mm charuco board whose position was altered in the meanwhile. First, each camera intrinsic parameter K and distortion coefficients d were calibrated from corresponding image sequence. Using 2D-2D correspondences about unique charuco board corners, relative pose of each camera pair $X_j = R_{ij}X_i + T_{ij}$, where R_{ij} is rotation matrix and T_{ij} is translation vector, in 4 camera can estimated. By fixing the first camera coordinate system as real world coordinate system, $R_1 = I_{3\times3}$, $T_1 = (0,0,0)^T$, poses of 4 camera were registered into real world coordinate system. A camera graph G with minimum degree $\delta(G) \geq 2$ is formed and tuned by bundle adjustment [Engels et al., 2006]. Once the 4 camera system got calibrated, the beans were released above the investigation volume and synchronized image sequences were captured with 150 fps.

Figure 1 describes the calibrated 4 camera system. A beam with real world coordinate (x, y, z) was captured by 4 cameras with corresponding image coordinates $(u_1, v1)$, (u_2, v_2), etc. Referring to pinhole camera model, the relationship between particle image coordinates and real world coordinates in homogeneous coordinate system is governed by

$$
\begin{bmatrix} u_i \\ v_i \\ 1 \end{bmatrix} = K_i \begin{bmatrix} R_i & T_i \end{bmatrix} \begin{bmatrix} x \\ y \\ z \\ 1 \end{bmatrix} = \begin{bmatrix} \overrightarrow{P_{i,1}} \\ \overrightarrow{P_{i,2}} \\ \overrightarrow{P_{i,3}} \end{bmatrix} \begin{bmatrix} x \\ y \\ z \\ 1 \end{bmatrix}, i = 1, 2, 3, 4, \tag{3}
$$

where $\overrightarrow{P_{i,i=j}}$ is j^{th} row vector of projection matrix P_i. Based on DLT algorithm [Shapiro, 1978], real word

particle position vector $\vec{X}$ can be solved by minimizing $\vec{w}$:

$$A\vec{X} = \begin{bmatrix} v_1\vec{p}_{1,3} - \vec{p}_{1,2} \\ \vec{p}_{1,1} - u_1\vec{p}_{1,3} \\ v_2\vec{p}_{2,3} - \vec{p}_{2,2} \\ \vec{p}_{2,1} - u_2\vec{p}_{2,3} \\ \vdots \end{bmatrix} = \vec{w} \approx 0, \tag{4}$$

where $\vec{w}$ is residue induced by noise. With SVD decomposition of A, $\vec{X}$ will be the corresponding column vector of V^T with smallest value of s. Due to weak matching between views for 2D particle detection, $\vec{X}$
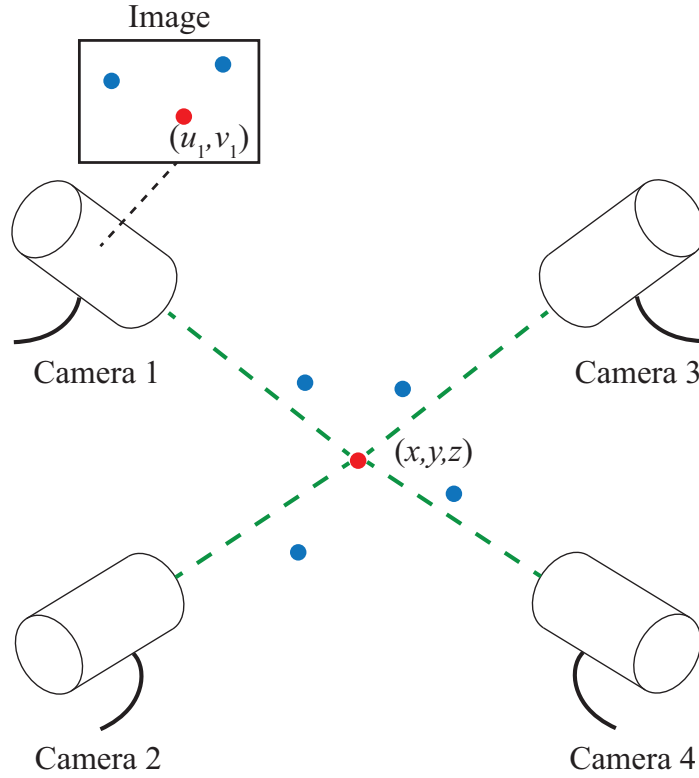

Figure 1: 4 view 3D particle reconstruction.

candidates and corresponding s were computed by DLT method with OpenMP optimized SIMD instruction. Ghost particle positions were removed according to descending order of s. Linking algorithm, proposed by Crocker and Grier [1996], was utilized to further remove outliers.

Result and Remark

This work achieved 4 view 3D particle tracking in large domain nearly instantaneously by removing majority of ghost particle during triangulation process. The basic principle about reconstruct particle based in N ($N = 4$) rays inspired following small scale particle tracking study.

Microscale Particle Tracking - Prototype

This Chapter is from the Journal Article: Hong, Liu, and Leonardo P. Chamorro. "A fast, non-iterative ray-intersection approach for three-dimensional microscale particle tracking." **Lab on a Chip** 22.5 (2022): 964-971.

In this work, we propose a non-iterative ray tracing method with robust post-capture microlens array sensor alignment to reconstruct sparse particle concentration in light field particle image velocimetry and particle tracking velocimetry nearly instantaneously. Voxels traversed by various rays are stored by kd-tree to reduce memory load and computational time. Cloud point classification algorithm is employed for particle identification and spatial reconstruction. The approach is tested with a physically-based realistic model of a light field camera. Also, an optical system is assembled in a microscope to directly obtain the 3D laminar velocity field in the fully-developed region, which exhibits good agreement with the theoretical solution.

Light Field Microscopy

Consider placing a microlens array in the intermediate image plane between a tube lens of an infinity-corrected microscope and a camera sensor to enable the microscope capturing light field in a single photograph [Levoy et al., 2006]; see a basic diagram in figure 2.

A 4D array $L(u, v, s, t)$ [Levoy and Hanrahan, 1996] describing the intersection of rays between sensor (u, v) and MLA (s, t) planes can be converted from a raw light field image. The sensor plane is located at the focal plane of MLA with a distance equal to the focal length of the lenslet f_l. The (u, v) coordinates are associated with pixels in each lenslet, encoding angular information. The (s, t) coordinates are associated with the center of each lenslet and encode spatial information. In each sub-image in (u, v) coordinates, the lenslet center is identified as origin (0,0).
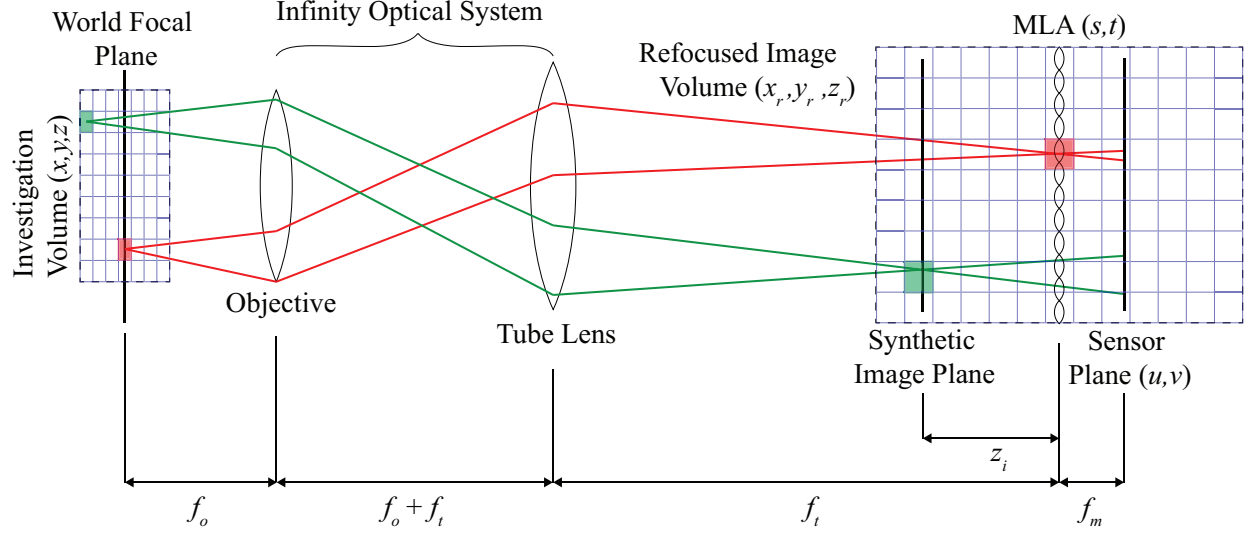
Figure 2: Schematics of a Light field system with an infinity-corrected microscope. Red lines indicate rays from in focus particle, whereas green lines denote those for an out-of-focus particle.

Due to it is not practical to perfectly align the lenslet center with a pixel in the camera sensor, pixels in each lenslet are interpolated onto a uniform (u, v) grid for computational efficiency. By decoding the 4D array $L(u, v, s, t)$, depth information can be recovered at the expense of spatial resolution [Levoy et al., 2006]. For this 3D reconstruction approach, the spatial resolution is modulated by the size of lenslet d_m, whereas the depth resolution is governed by the sub-image resolution $N_s = d_m/d_p$, where d_p is the pixel size. Once 2D raw light field images are reshaped to a 4D array, 3D intensity distribution can be calculated using algebraic or 3D convolution methods.

Since the majority of pixels do not receive rays from the particles and PIV/PTV only need to reconstruct the location of the particles, rays unit vector pre-filtered data matrix Q (Equation 5) and rays counter matrix $C(x_r, y_r, z_r)$ are introduced to reduce the computational load. A simple intensity threshold filter computed based on raw images without particles may be used to binarize light field images to select pixels lit by particles to form

$$Q = \begin{bmatrix} | & | & | & | & | \\ x_p & y_p & \hat{i} & \hat{j} & \hat{k} \\ | & | & | & | & | \end{bmatrix}, \quad Q \in C^{M \times 5} \tag{5}$$

where M indicates the number of rays used for ray tracing, (x_p, y_p) is the pixel coordinates on the sensor and $(\hat{i}, \hat{j}, \hat{k})$ is the unit direction vector given by connecting the pixel and its corresponding lenslet center treated as a pinhole.

Then, the 3D reconstruction of particles can be converted to an "intersection points" finding problem

(figure 3a) of 3D skew lines (Rays). The refocused image volume is discretized into small voxels, and the ray counter matrix $C(x_r, y_r, z_r)$ is zero-initialized to solve this problem. Since all rays are nearly perpendicular to the (x, y) plane, we consider that a ray can be conceptualized as passing through the voxel if it intersects with the center plane of the voxel (figure 3b) to accelerate calculation. The spatial coordinates of intersected points for rays with different depth center planes can be computed as follows:

$$\begin{bmatrix} x_p' \\ y_p' \end{bmatrix} = \frac{z_r}{\hat{k}} \begin{bmatrix} \hat{i} \\ \hat{j} \end{bmatrix} + \begin{bmatrix} x_p \\ y_p \end{bmatrix} \tag{6}$$

Using a binary search, the rays counter of the closest voxel (x_r, y_r, z_r) of the intersection point (x_p', y_p', z_r) is incremented by one. The counting is performed with atomic operation in GPU's shared memory to reduce processing time (figure 3b). The ray counter matrix $C(x_r, y_r, z_r)$ is filtered by half of the number of pixels lit by a particle in-focus plane to avoid noncritical cloud point processing; it is computed as

$$C_{min} = \lfloor \frac{1}{2}(R_p \times M/q)^2 \pi \rfloor, \tag{7}$$

where $\lfloor x \rfloor$ is the floor function, M is the magnification of the objective lens, R_p is the radius of the particle, and q is the pixel size. Then, according to the particle density in the discretized refocused image volume, sparse voxels with ray counters can be classified and further reduced to a one-to-one correspondence between particles and voxels. If points cloud are relative dense, voxels with local maximum ray counters are screened with a fast nearest neighbor search of kd tree [Ramasubramanian and Paliwal, 1989]. Otherwise, density-based spatial clustering of application with noise, DBSCAN [Ester et al., 1996] is utilized to classify voxels, and the center positions are computed via averaging throughout classes. See the illustrative flowchart in figure 4.
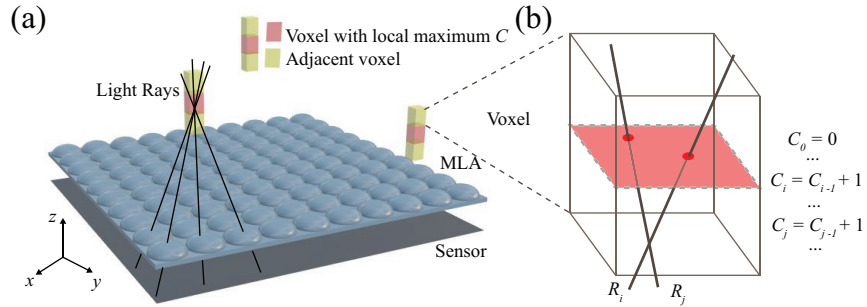

Figure 3: (a) 3D light ray diagram of an image volume around the microlens array, MLA; (b) increment of ray counter in one voxel.
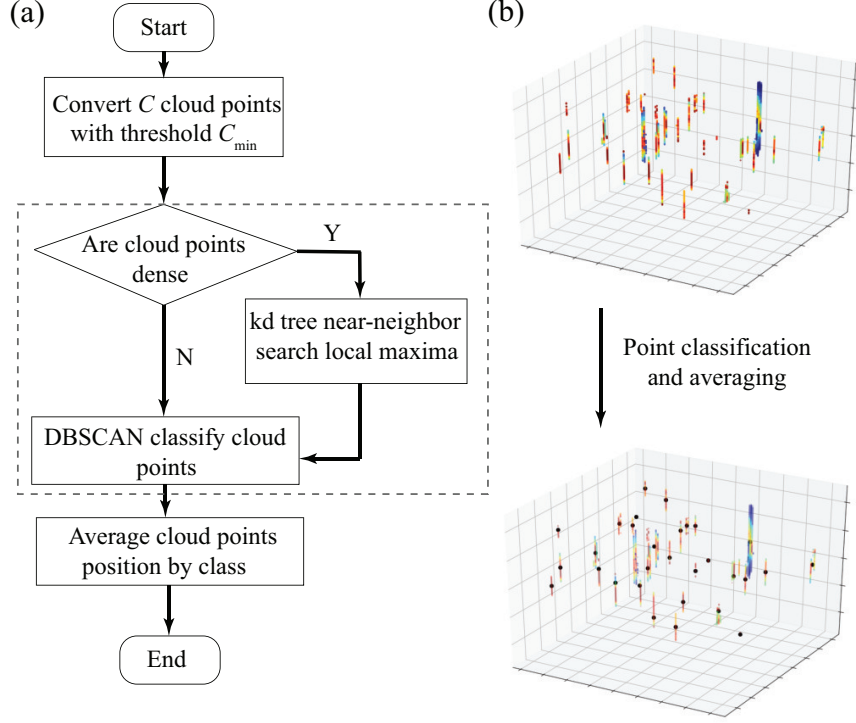
(a)

```
        Start
          │
          ▼
  ┌──────────────────┐
  │ Convert C cloud points │
  │  with threshold C_min  │
  └──────────────────┘
          │
┌─────────┼──────────────────────────┐
│         ▼                           │
│    ◇ Are cloud points ◇──── Y ──┐   │
│      dense                      │   │
│         │                       ▼   │
│         N          ┌──────────────────┐
│         │          │ kd tree near-neighbor │
│         │          │ search local maxima   │
│         ▼          └──────────────────┘
│  ┌──────────────────┐       │
│  │ DBSCAN classify cloud │◄──┘
│  │       points          │
│  └──────────────────┘
└──────────┼──────────────────────────┘
           ▼
   ┌──────────────────┐
   │ Average cloud points │
   │  position by class   │
   └──────────────────┘
           │
           ▼
          End
```

(b)

Point classification and averaging

Figure 4: (a) Cloud point classification and center position calculation flowchart; (b) 3D cloud point for particle center position calculation.

Ray simulation

Now, we introduce a physically-based simulation [Michels et al., 2018] with a realistic lens to compare the ground truth with a refocused position of particles. An $f/2.0 \pm 22°$ double-Gaussian camera lens is constructed in Blender, as shown in figure 5a. All the surfaces of the objective lens are discretized into 64 radial and 128 longitudinal vertices to achieve an approximately round surface, and a material shader is used for normal surface correction. Details of this particular lens can be found in Smith [2005]. With 2D Ray simulation in Zemax, the optic system can be treated as a thick convex lens with two cardinal planes H_1, H_2 as illustrated in figure 5b. The scattered light from an object in position A has a corresponding image position A' calculated as follows:

$$\frac{1}{EFL} = \frac{1}{s'} + \frac{1}{s} \tag{8}$$

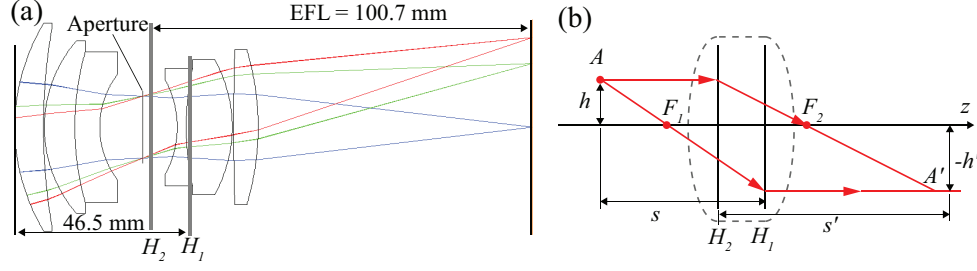$$\begin{bmatrix} x_i \\ y_i \end{bmatrix} = \frac{s'}{s} \begin{bmatrix} x \\ y \end{bmatrix} \tag{9}$$

Figure 5: (a) Schematics of the double-Gaussian camera model with MLA; (b) an equivalent thick convex lens with two cardinal planes, H_1 and H_2.
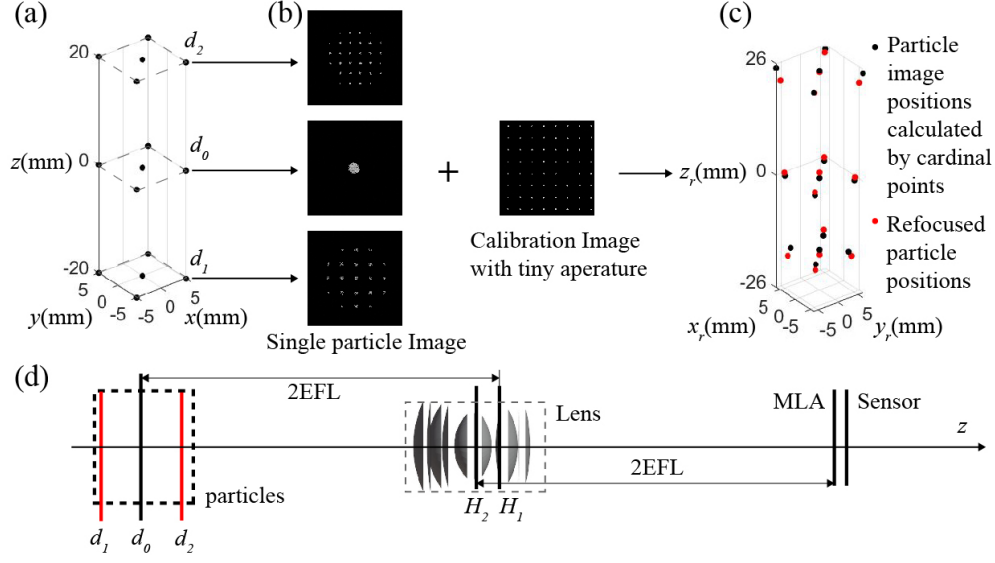

Figure 6: Configuration of LF simulation for uncertainty analysis of 3D particle reconstruction. (a) Three layers of particles in the objective space; (b) corresponding LF images; (c) reconstruction with ground truth; (d) Simulation details.

where EFL is the effective focal length. All other parameters used in this simulation are based on the experiment's device to compare with a real experimental setup. A rectangular MLA with pitch $p_m = 125$ μm and focal length $f_m = 3.75$ mm is placed at $2EFL$ behind the H_2 plane. The curvature radius R_1 of each lenslet of the MLA with negligible thickness of backplate, $d \approx 0$, and flat backplane, $R_2 = \infty$, is computed based on the lens maker's equation

$$\frac{1}{f_m} = (n-1)\left(\frac{1}{R_1} - \frac{1}{R_2} + \frac{(n-1)d}{nR_1R_2}\right) = \frac{n-1}{R_1}. \tag{10}$$

Here, $n = 1.56$ is the index of refraction, IOR, according to the MLA material (MLA-S125-f30) used in the experiment. A 35.9 mm × 23.9 mm camera sensor with 8256 pixels × 5504 pixels (Nikon D850), is placed on the focal plane of the MLA as shown in figure 6d.

Spherical particles of radius $r = 30$ μm are placed at various depths z, namely, d_0, d_1, and d_2 in figure 6d) with a distance of around $2EFL$ from the H_1 plane. Based on equation 8, the in-focused particles image is located in the MLA plane. Emission shade is added to the particle's surface to simulate light reflection or emission in a real experiment. By using implemented cycles render engine, 2048 render samples per pixel are computed with GPU. Three raw LF images are rendered corresponding to 15 particles on the d_0, d_1 and d_2 planes. Figure 6a shows the particle positions in the objective volume, and figure 6b shows the raw counterpart. Then, a calibration image is rendered by creating an area light source on d_0 and reducing the aperture size of the main lens to a sufficiently small value.

The image volume is discretized into 125 μm (x) × 125 μm (y) × 250 μm (z) voxels and the corresponding ray counter matrix $C(x_r, y_r, z_r)$ is initialized. Finally, the 3D particle positions are reconstructed to voxels in the image volume and compared with theoretical image positions calculated from equation 8 and 9; see figure 6c. The mean error distance in image volume is 1.24 mm; it is caused by lateral resolution, limited angular resolution, radial distortion, depth distortion, vignetting, and the limited number of simulated rays. However, high magnification and tele-centricity (orthographic views) of the macro lens and microscopes can reduce distortion induced by the lens. All rays that go through MLA are recorded by pixels in the real experiment. The distance error in object volume should be recomputed based on the lens magnification, M, i.e.,

$$\Delta x = \frac{\Delta x_i}{M}, \Delta y = \frac{\Delta y_i}{M}, \Delta z = \frac{\Delta z_i}{M^2} \tag{11}$$

where Δx_i, Δy_i, and Δz_i are distance errors in the image volume, whereas Δx, Δy, and Δz are distance errors in the object volume. For instance, with a 20X objective lens, 1.24 mm distance error under a large lens distortion leads to an only upper bound of 10.6 μm distance error (around $10R_p$) in the objective volume. The distance error of particle 3D reconstruction of the microscope is much smaller compared to the simulation case.

Experiment - Proof of concept

3D PIV is conducted in a rectangular micro channel of 200 μm × 200 μm cross-section and × 58.5 mm long; see basic schematics in figure 7a. The system uses a Nikon Eclipse Ti2 inverted microscope, which utilizes fluorescence filter cubes to capture high signal-to-noise ratio images. A Nikon CFI Plan Fluor 20X/0.5 objective lens is used to provide high contrast fluorescence observation, and a 45.4 megapixel Nikon D850 camera (pixel size $p = 4.35$ μm) with nose-to-nose 50 mm f/1.8D lenses is employed to capture 1:1 images with large aperture. A 25.4 mm round MLA (RPC photonics S125-f30) contains lenslets with pitch size $p_l =$

125 μm and focal length $f_m = 3.75$ mm. A continuous 532 nm laser is used to illuminate the interrogation volume through a dichroic filter cube and objective lens. The seeding consists of 1.7-2.2 μm fluorescent Nile Red particles (Spherotech), whose emission spectral peak is around 560 nm. A high-pass filter in the cube blocks the reflections of the laser light and allows emission light from particles capture from the camera. A programmable Harvard syringe pump pumps a distilled water-particle solution to the microchannel through microtubes at a flow rate of 0.85 μl/min (equivalent to a Reynolds number of $Re \approx 0.07$). Thirty-five images are captured at a low frame rate of 7 Hz with DX-format, 300 μs exposure and 25600 ISO to maximize image resolution without binning. See a diagram and photograph of the setup in figure 7.

This configuration implies a minimum number of spots behind each lenslet $N_u \approx 23.7$ [Levoy et al., 2006], which is calculated as,

$$N_u = \frac{p_l}{R_{obj}}, R_{obj} = \frac{0.47\lambda}{NA}M \tag{12}$$

where λ is the emission wavelength of fluorescent particles, NA is numerical aperture, M is magnification of objective lens and R_{obj} is the Sparrow limit for the smallest spacing between two distinguishable spots in the specimen [Inoué, 2013]. The number of pixels in one lenslet, $p_l/p \approx 28.7$, is larger than N_u to ensure the pixel density does not limit the angular resolution. N_u can also be regarded as the number of slices in the depth direction, leading to a depth resolution $D_{tot_2} \approx 28.8$ μm and a total reconstruction depth $D_V \approx 680$ μm [Levoy et al., 2006], which are computed as,

$$D_{tot_2} \approx \frac{(2 + N_u)\lambda n_m}{2NA^2}, D_V \approx N_u D_{tot_2} \tag{13}$$

where n_m is refractive index of the medium. To simplify the problem and to avoid under-sampling, the depth length of voxel for image volume is set to $\Delta z_r \approx D_{tot_2}M^2/3 \approx 4$ mm. Furthermore, Δz_r (≈ 4 mm) also prevents reconstruction from virtual image since it is larger than f_m.

Result and Discussion

The LF 3D$-\mu$PIV is compared with the theoretical fully-developed laminar solution for the flow rate of 0.85 μl/min. Figure 8a illustrates velocity profile colored with velocity magnitude. A comparison of the velocity profiles along the major diagonals are shown in figure 8b,c. The maximum velocity magnitude from the experiment match well with the theoretical prediction. However, some departures are attributed to image plane too close to the MLA plane. Shorter f_m offers more accurate reconstruction around the MLA plane, but it sacrifices depth of view. Furthermore, high particle velocity in center region also destabilizes the
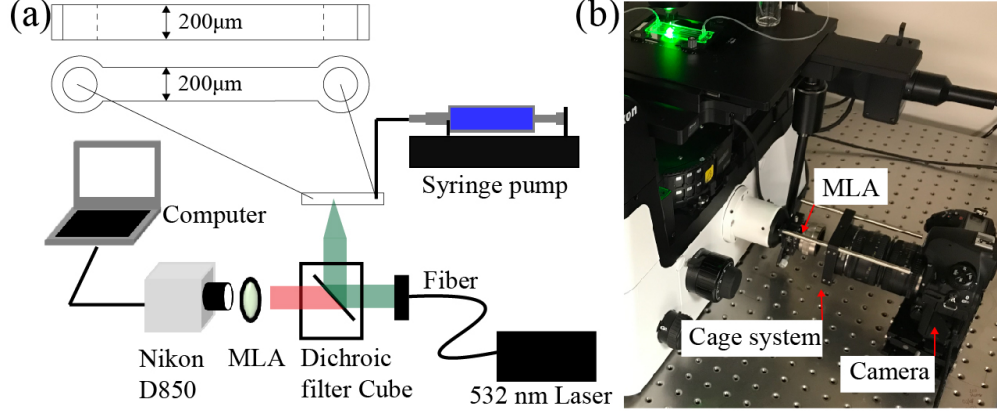
Figure 7: (a) General schematic of the microchannel and experimental setup; (b) photograph of the pre-calibrated MLA cage system by placing the MLA into intermediate image plane between 1:1 DSLR camera and microscope.

linking algorithm, which may also affect estimation of the velocity field. Finally, the relative measurement error is calculated as

$$e(y, z) = \frac{|u_{exp}(y, z) - u_{theo}(y, z)|}{u_{theo}(y, z)} \times 100 \tag{14}$$

where $u_{exp}(y, z)$, $u_{theo}(y, z)$ are velocity profile based on experiment and theoretical prediction. As a result, the relative error is around 5% in the corner region and 12 % at the center. Overall, the bulk flowrate is estimated as 0.834 μm/min, close to the experimental flowrate of 0.85μm/min.
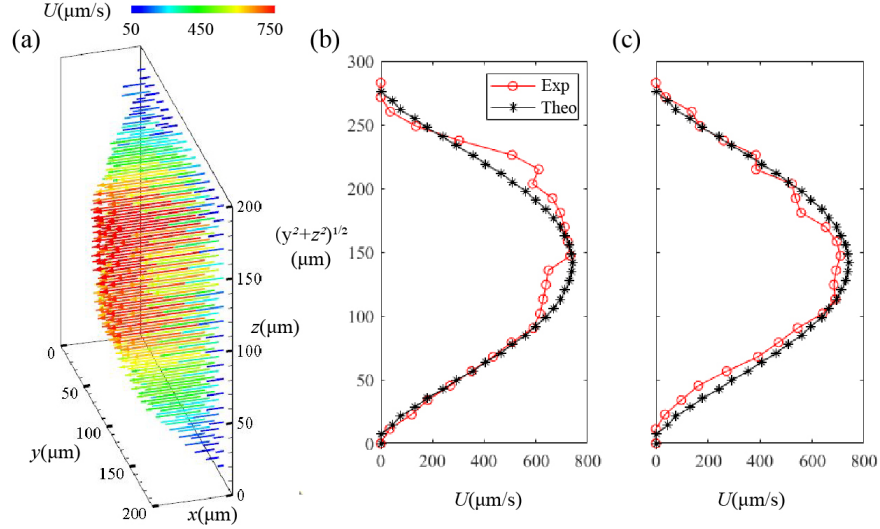

Figure 8: (a) A view of the velocity distribution; (b) comparison of the measured velocity profile along the $y - z$ diagonal direction with theoretical profile; (c) same as b) but in the other diagonal.

Cm-scale 3D Particle Tracking - Propose

Multi-camera-based flow description in Eulerian and Lagrangian frames of reference at mm and cm scales is usually challenging due to shallow depth of field (DOF) from macro lenses and calibration procedures. I want to improve the rapid 3D particle tracking system described in above chapter for cm-scale volume application with perspective view. With the use of a microlens array (MLA) in the intermediate plane between the macro lens and camera sensor (Figure 9), light field information can be obtained by a single camera cage system without stereo calibration. A fast ray intersection and cloud point classification method with GPU acceleration is applied to reconstruct 3D particle position in a uniformly discretized image space and then mapped to non-uniform objective space based on macro lens properties. With atomic operation within the onboard memory of GPU, the processing time per image can be under one second. Lagrangian particle tracking Crocker-Grier method is used for particle linking to characterize time-resolved flow field.
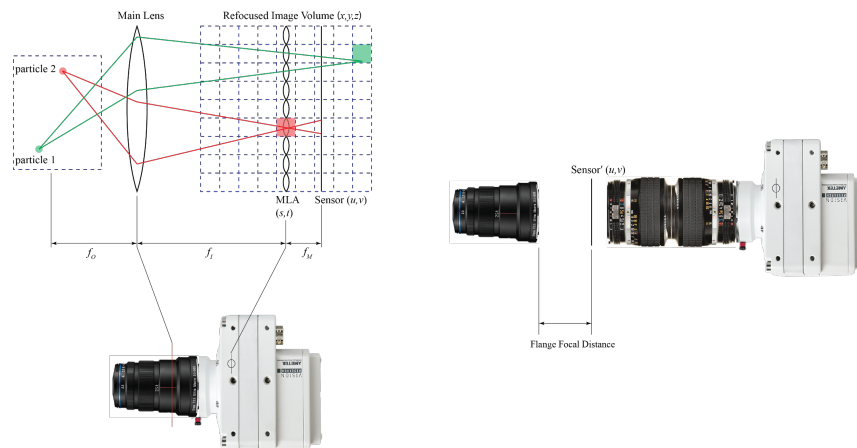

Figure 9: Light field system with 25mm $f/2.8$ $2.5 \times$ macro lens.

1. Parallelized Ray Counting - pursue real-time tracking

For cm-scale sparse particle tracking, providing near-instantaneous tracking result is essential function to apply this method to many applications such as controllable flow structure interactions, detection of micro-organism activities and so on. I decided to squeeze the power of modern processor to pursue real-time tracking. Figure 10 shows the raw LF images can be reorganized as 4 D matrix, each row will represent one pixel, which can be processed by single thread. Hence every pixel in each image will be processed simultaneously to reduce the reconstruction time. Consider the memory transfer latency, target volume is discretized into $400 \times 200 \times 150$ voxels, 3D reconstruction time for single frame is compared for SIMD, OpenMP, MPI, CUDA method (Figure 11). GPU-based parallel computing is as efficient as MPI method, but it can be executed in desktop instead of multi-nodes on super cluster.
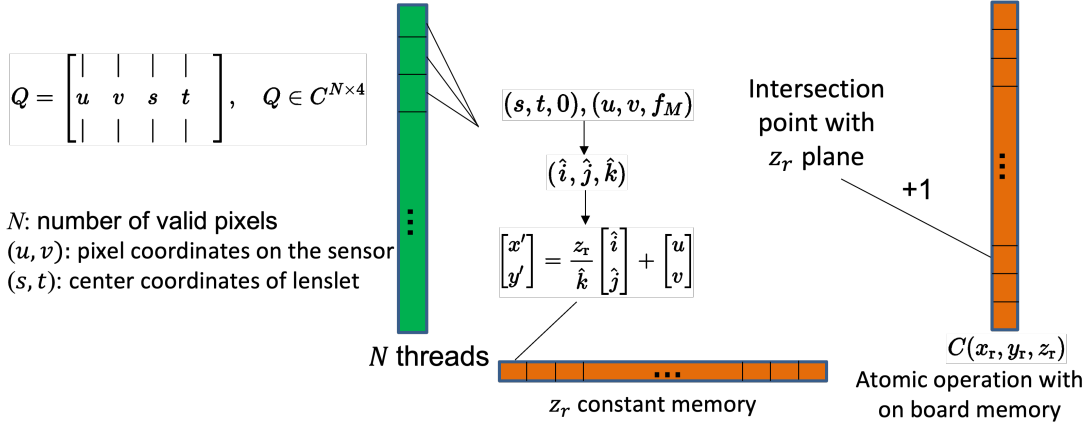

Figure 10: Parallelized computing in GPU.

The future plan of this part is combine parallelized reconstruction step with updated classification step and tree searching step (Figure 4)to achieve real-time tracking.

2. Lens Distortion - perspective view

Compared to orthographic imaging system (microscopy), perspective zoom lens introduces larger lens distortion due to relative short effective focal length (EFL). Figure 12 reveals that when approach to the edge of images, we can't use center of circle to represent the lenslet center in Zoom lens image due to significant distortion. For microscopical system, this distortion can be calibrated by reducing condense aperture size (Figure 13). However, tuning aperture size of Zoom lens system will introduce pixel level displacement between elements in optical train, which will destroy the calibration. For this part, a image processing based
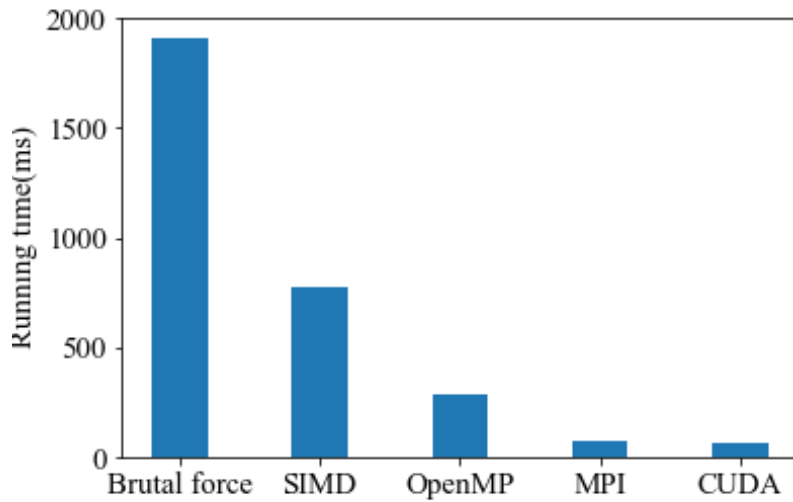
Figure 11: Computation time for SIMD, OpenMP, MPI, CUDA method.

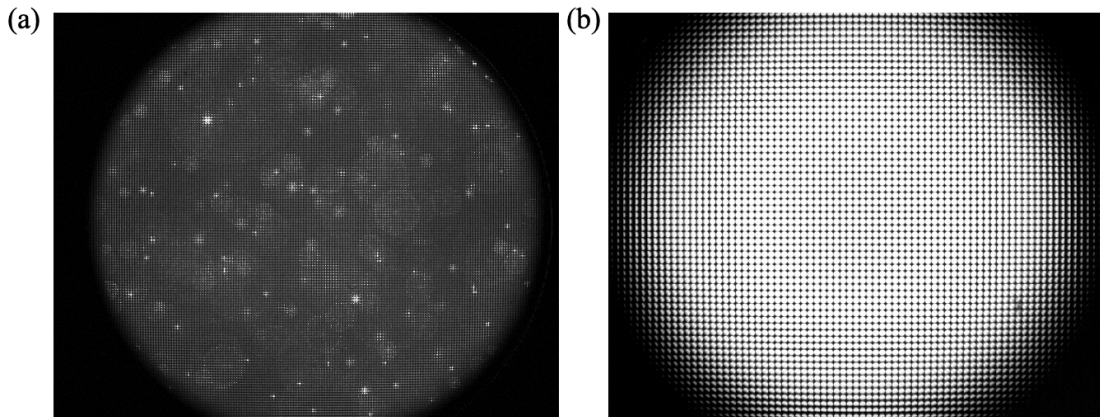calirbation will be developed to elimite distorted subimages and indentify lenslet center.

Figure 12: (a) Orthographic calibration; (b) Zoom lens calibration.

3. Simulation

In order to understand uncertainty in perspective view system, a physically-based simulation is inevitable. Based on $f/2.8$, 2.5 zoom-ratio Venus Laowa macro lens, which will be used in future experiment, we constructed a 12 elements $f/2.8$, 2.5 zoom-ratio macro lens (Figure 14) [Smith, 2005] to perform particle reconstruction. With both 2D Zemax and 3D blender simulation, the uncertainty of short focal macro lens will be characterized.
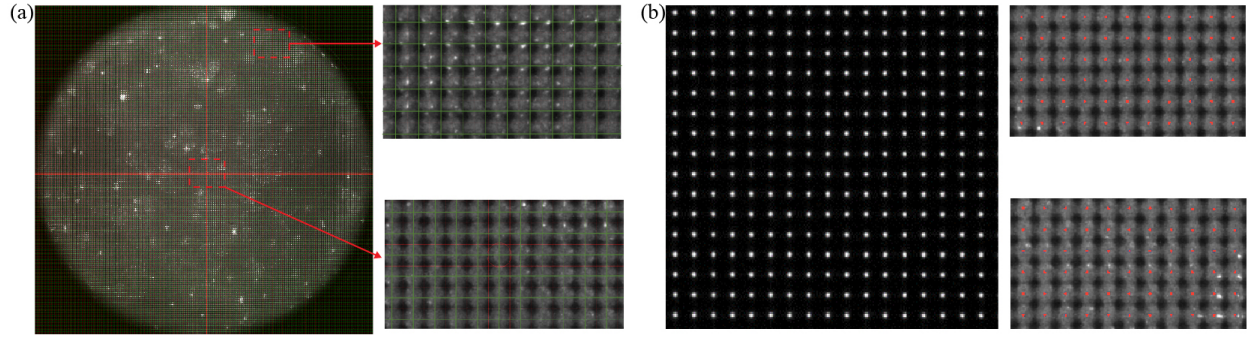
Figure 13: (a) An MLA grid overlaid on the image-based on the center alignment (grid points are center of each lenslet); (b) calibration images with small condenser aperture size, leading to precise micro image identification everywhere on the image (red points indicate the center of each lenslet).

4. Experiment

We will use this approach to study the flow induced by oscillated boundary. Resonance speakers will be used to shake the boundary wall with various frequency and particle motion in 7mm $\times$ 7mm $\times$ 7mm volume will be captured by this LF camera system.
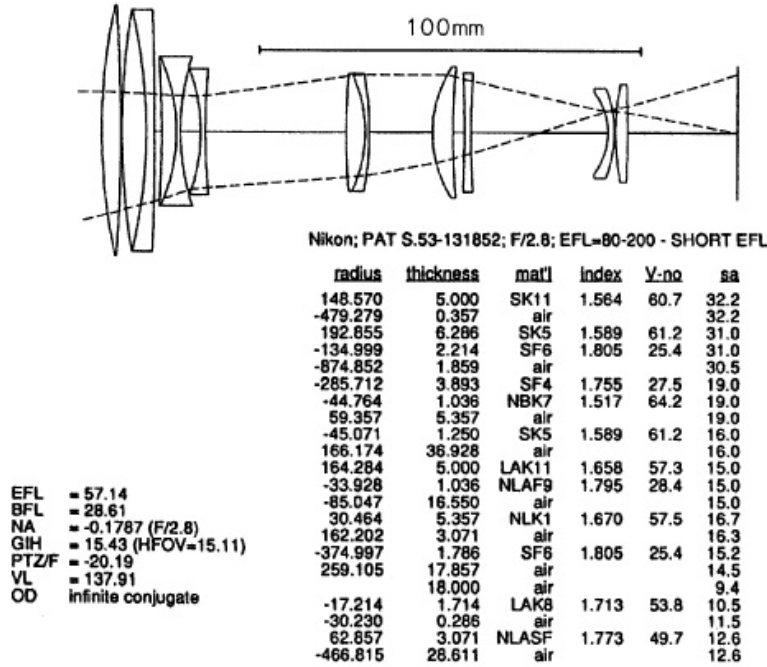
Figure 14: 12-elements short focal macro lens.

References

Edward H Adelson and John YA Wang. Single lens stereo with a plenoptic camera. *IEEE transactions on pattern analysis and machine intelligence*, 14(2):99–106, 1992.

Edward H Adelson, James R Bergen, et al. *The plenoptic function and the elements of early vision*, volume 2. Vision and Modeling Group, Media Laboratory, Massachusetts Institute of . . . , 1991.

Gwon Hwan An, Siyeong Lee, Min-Woo Seo, Kugjin Yun, Won-Sik Cheong, and Suk-Ju Kang. Charuco board-based omnidirectional camera calibration method. *Electronics*, 7(12):421, 2018.

Jesse Belden, Tadd T Truscott, Michael C Axiak, and Alexandra H Techet. Three-dimensional synthetic aperture particle image velocimetry. *Meas Sci Tech*, 21(12):125403, 2010.

MR Bown, JM MacInnes, RWK Allen, and WBJ Zimmerman. Three-dimensional, three-component velocity measurements using stereoscopic micro-piv and ptv. *Meas Sci Tech*, 17(8):2175, 2006.

John C Crocker and David G Grier. Methods of digital video microscopy for colloidal studies. *Journal of colloid and interface science*, 179(1):298–310, 1996.

Mustafa Ugur Daloglu, Wei Luo, Faizan Shabbir, Francis Lin, Kevin Kim, Inje Lee, Jia-Qi Jiang, Wen-Jun Cai, Vishwajith Ramesh, Meng-Yuan Yu, et al. Label-free 3d computational imaging of spermatozoon locomotion, head spin and flagellum beating over a large volume. *Light: Science & Applications*, 7(1): 17121–17121, 2018.

Chris Engels, Henrik Stewénius, and David Nistér. Bundle adjustment rules. *Photogrammetric computer vision*, 2(32), 2006.

Martin Ester, Hans-Peter Kriegel, Jörg Sander, Xiaowei Xu, et al. A density-based algorithm for discovering clusters in large spatial databases with noise. In *kdd*, volume 96, pages 226–231, 1996.

Timothy W Fahringer, Kyle P Lynch, and Brian S Thurow. Volumetric particle image velocimetry with a single plenoptic camera. *Meas Sci Tech*, 26(11):115201, 2015.

Andreī Gershun. The light field. *J Math Phys Camb*, 18(1-4):51–151, 1939.

Gabor T Herman and Arnold Lent. Iterative reconstruction algorithms. *Comput Biol Med*, 6(4):273–294, 1976.

Klaus D Hinsch. Holographic particle image velocimetry. *Meas Sci Tech*, 13(7):R61, 2002.

Hideaki Hisamoto, Takayuki Horiuchi, Manabu Tokeshi, Akihide Hibara, and Takehiko Kitamori. On-chip integration of neutral ionophore-based ion pair extraction reaction. *Anal Chem*, 73(6):1382–1386, 2001.

Shinya Inoué. *Video microscopy*. Springer Science & Business Media, 2013.

Pushyami Kaveti and Hanumant Singh. A light field front-end for robust slam in dynamic environments. *arXiv preprint arXiv:2012.10714*, 2020.

Haruyuki Kinoshita, Shohei Kaneda, Teruo Fujii, and Marie Oshima. Three-dimensional measurement and visualization of internal flow of a moving droplet using confocal micro-piv. *Lab Chip*, 7(3):338–346, 2007.

Johannes Kluge, Francesco Fusaro, Nathalie Casas, Marco Mazzotti, and Gerhard Muhrer. Production of plga micro-and nanocomposites by supercritical fluid extraction of emulsions: I. encapsulation of lysozyme. *J Supercrit Fluid*, 50(3):327–335, 2009.

Marc Levoy and Pat Hanrahan. Light field rendering. In *Proceedings of the 23rd annual conference on Computer graphics and interactive techniques*, pages 31–42, 1996.

Marc Levoy, Ren Ng, Andrew Adams, Matthew Footer, and Mark Horowitz. Light field microscopy. In *ACM SIGGRAPH 2006 Papers*, pages 924–934. 2006.

H Li, J Ding, Z Zhao, W Qu, J Xiong, and S Shi. Investigation of 3d flow behaviour inside a 3×3 rod bundle using light field-piv and the matched refractive index techniques. In *The 12th international symposium on particle image velocimetry. Busan, Korea*, 2017.

Rui Lima, Shigeo Wada, Shuji Tanaka, Motohiro Takeda, Takuji Ishikawa, Ken-ichi Tsubota, Yohsuke Imai, and Takami Yamaguchi. In vitro blood flow in a rectangular pdms microchannel: experimental observations using a confocal micro-piv system. *Biomed Microdevices*, 10(2):153–167, 2008.

Ralph Lindken, Jerry Westerweel, and Bernhard Wieneke. Stereoscopic micro particle image velocimetry. *Exp Fluids*, 41(2):161–171, 2006.

Ying Zheng Liu, Byoung Jae Kim, and Hyung Jin Sung. Two-fluid mixing in a microchannel. *Int J Heat Fluid FL*, 25(6):986–995, 2004.

Kyle Lynch, Tim Fahringer, and Brian Thurow. Three-dimensional particle image velocimetry using a plenoptic camera. In *50th AIAA Aerospace Sciences Meeting including the New Horizons Forum and Aerospace Exposition*, page 1056, 2012.

Pasquale Memmolo, Andrea Finizio, Melania Paturzo, Lisa Miccio, and Pietro Ferraro. Twin-beams digital holography for 3d tracking and quantitative phase-contrast microscopy in microfluidics. *Opt Express*, 19 (25):25833–25842, 2011.

Tim Michels, Arne Petersen, Luca Palmieri, and Reinhard Koch. Simulation of plenoptic cameras. In *2018-3DTV-Conference: The True Vision-Capture, Transmission and Display of 3D Video (3DTV-CON)*, pages 1–4. IEEE, 2018.

Ren Ng. Fourier slice photography. In *ACM SIGGRAPH 2005 Papers*, pages 735–744. 2005.

Nam-Trung Nguyen, Seyed Ali Mousavi Shaegh, Navid Kashaninejad, and Dinh-Tuan Phan. Design, fabrication and characterization of drug delivery systems based on lab-on-a-chip technology. *Adv Drug Deliver Rev*, 65(11-12):1403–1419, 2013.

TA Ooms, R Lindken, and J Westerweel. Digital holographic microscopy applied to measurement of a flow in a t-shaped micromixer. *Exp Fluids*, 47(6):941–955, 2009.

Francisco Pereira, Jian Lu, Emilio Castano-Graff, and Morteza Gharib. Microscale 3d flow mapping with μddpiv. *Exp Fluids*, 42(4):589–599, 2007.

Horst Piller. *Microscope photometry*. Springer Science & Business Media, 2012.

V Ramasubramanian and KK Paliwal. A generalized optimization of the kd tree for fast nearest-neighbour search. In *Fourth IEEE Region 10 International Conference TENCON*, pages 565–568. IEEE, 1989.

Daniel Schanz, Sebastian Gesemann, and Andreas Schröder. Shake-the-box: Lagrangian particle tracking at high particle image densities. *Experiments in fluids*, 57:1–27, 2016.

Robert Shapiro. Direct linear transformation method for three-dimensional cinematography. *Research Quarterly. American Alliance for Health, Physical Education and Recreation*, 49(2):197–205, 1978.

Jian Sheng, Edwin Malkiel, and Joseph Katz. Digital holographic microscope for measuring three-dimensional particle distributions and motions. *Appl optics*, 45(16):3893–3901, 2006.

Shengxian Shi, Jianhua Wang, Junfei Ding, Zhou Zhao, and TH New. Parametric study on light field volumetric particle image velocimetry. *Flow Meas Instrum*, 49:70–88, 2016a.

Shengxian Shi, Junfei Ding, Tze H New, and Julio Soria. Light-field camera-based 3d volumetric particle image velocimetry with dense ray tracing reconstruction technique. *Exp Fluids*, 58(7):1–16, 2017.

SX Shi, Junfei Ding, and TH New. Dense ray tracing based reconstruction algorithm for light field piv and comparative study with tomo-piv. In *18th International Symposium on the Application of Laser and Imaging Techniques to Fluid Mechanics*, 2016b.

Jean-Baptiste Sibarita. Deconvolution microscopy. *Adv Biochem Eng Biot*, pages 201–243, 2005.

Vishal Singhal, Suresh V Garimella, and Arvind Raman. Microscale pumping technologies for microchannel cooling systems. *Appl Mech Rev*, 57(3):191–221, 2004.

Warren J Smith. Modern lens design. 2005.

Helen Song and Rustem F Ismagilov. Millisecond kinetics on a microfluidic chip using nanoliters of reagents. *J Am Chem Soc*, 125(47):14613–14619, 2003.

Julio Soria and Callum Atkinson. Towards 3c-3d digital holographic fluid velocity vector field measurement—tomographic digital holographic piv (tomo-hpiv). *Meas Sci Tech*, 19(7):074002, 2008.

Michael W Tao, Sunil Hadap, Jitendra Malik, and Ravi Ramamoorthi. Depth from combining defocus and correspondence using light-field cameras. In *Proceedings of the IEEE International Conference on Computer Vision*, pages 673–680, 2013.